International Journal of
Automotive Manufacturing and Materials (IJAMM)

Article

Study on Gas Flow Characteristics in Automobile Micro Gas Sensors

Longkang Han [1], Feng Han [2,*], Ruquan Liang [2], Jianhui Shi [2], Dengbo Zhang [2],
Yuanmei Song [2], and Kun Sun [3]

[1] School of logistics, Linyi University, Linyi 276000, China
[2] School of Mechanical and Vehicle Engineering, Linyi University, Linyi 276000, China
[3] School of Mechatronics Engineering, Anhui University of Science and Technology, Huainan 232001, China
* Correspondence: hanfeng@lyu.edu.cn
Received: 25 July 2024; Revised: 14 August 2024; Accepted: 22 August 2024; Published: 5 September 2024

Abstract: Micro gas sensors are integral to the automotive industry, particularly for monitoring the behavior of rarefied gases. The occurrence of inhomogeneous temperature gradients across microchannels can initiate gas flow, a principle that can be effectively utilized to develop micro gas sensors for automotive applications. This manuscript presents a novel microchannel design that incorporates quadrilateral sections with distinct temperature profiles. The characteristics of gas flow within this microchannel have been simulated numerically through the Direct Simulation Monte Carlo (DSMC) method, a sophisticated approach for such analyses. Subsequently, an optimization study is conducted to characterize the gas pumping properties of the microchannel. The results demonstrate that gas preferentially moves from a quadrilateral with lower temperature to one with higher temperature. The validity of this gas flow within the microchannel is confirmed. Notably, the gas flow velocity peaks at a Knudsen number of 3. This condition corresponds to a transitional flow regime, indicating that the microchannel's gas pumping capability is most robust during this phase. Furthermore, it is observed that an increase in the quadrilateral aspect ratio leads to a reduction in gas flow velocity. These results can be applied to design micro gas sensors for various industry fields.

Keywords: micro gas sensors; microchannel; Direct Simulation Monte Carlo (DSMC) method; thermally induced flow

1. Introduction

Micro gas sensors have a variety of applications in the automotive industry. In exhaust emission monitoring, micro gas sensors can be used to monitor the oxygen content and nitrogen oxide (NO_x) concentration in automobile exhaust gases. Oxygen sensors help the engine control module (ECM) adjust fuel injection to reduce harmful emissions by detecting the oxygen content in the exhaust gas [1]. In terms of in-vehicle air quality monitoring, micro gas sensors can also be used to monitor in-vehicle air quality, such as detecting CO_2 concentration [2]. In terms of new energy vehicle battery safety monitoring, micro gas sensors, such as MEMS hydrogen sensors, are capable of monitoring hydrogen energy gases with high sensitivity, high selectivity, and fast response, providing early warning for automotive power batteries to safeguard the lives and properties of passengers [3,4].

In rarefied gases, inhomogeneous temperature gradients within microchannels can induce a gas flow known as thermally induced flow. Due to the thermally induced flow, such microchannels can be used as micro gas sensors in automotive applications. Thermally-induced flows can be categorized into thermal creep flows [5,6], thermal edge flows [7,8], radiometric flows [9–11], and thermal-creep-like flows [10,12] based on their generation mechanisms. Thermal creep flow arises near a wall that experiences a temperature gradient, prompting gas molecules to migrate from cooler regions toward warmer zones. On the other hand, thermal edge flow is triggered near the periphery of a high-temperature plate, causing a directional movement of gas molecules towards the plate's edge. Radiometric flow occurs near a plate with dissimilar temperatures on either side, resulting in a flow of gas molecules from the colder side to the warmer side, circumventing the plate's edge. Lastly, thermal-creep-like flow is generated near two adjacent walls with differing temperatures, with gas molecules transferring from the colder to the warmer side.

Various configurations of microchannels have been proposed based on different thermally induced flow mechanisms. Among these, microchannel configurations with thermal creep flow as the mechanism are the most abundant. Aoki et al. [13] proposed a simple, smooth, and curved microchannel. Further, Bond et al. [5,14] proposed double-curved, sinusoidal, and matrix array microchannels. Donkov et al. [15] proposed a microchannel with two surfaces in the patterns of a flat plate and a ratchet, while Würger [16] suggested a microchannel with both surfaces in the patterns of ratchet. Chen et al. [17, 18] studied a microchannel with asymmetric ratchet patterns on two surfaces. Shahabi et al. [19] investigated different accommodation coefficients of the alternating ratchet patterns for the microchannels. Later, microchannels based on linear diverging or converging cross sections [20] and polymer membranes [21] in different pore sizes were reported. In addition, microchannel configurations with radiometric flow as the mechanism were proposed. Lotfian and Roohi [10] studied three categories of radiometric pumps featuring vane and ratchet geometries on the bottom or top surfaces of microchannels. Inspired by the Crookes radiometer, Baier et al. [11] proposed a microchannel having an array of small plates evenly arranged along the microchannel direction. Han et al. [22] carried out a study on the application of radiometric flow-type microchannels for gas separation and investigated the effect of intermolecular collision processes [23] and collision processes between molecules and surfaces [24] on the gas separation characteristics. For the microchannel with thermal edge flow as the mechanism, Wang et al. [25] proposed a microchannel with triangles uniformly arranged inside the microchannel and carried out the study of gas flow characteristics. Yakunchikov and Kosyanchuk [8] proposed a filament array-type microchannel with different temperatures inside the microchannel. The effects of Knudsen number and geometrical configuration on the gas flow characteristics were investigated. For microchannels with thermal-creep-like flow as the mechanism, Han et al. [26] proposed a microchannel with quadrilateral arrays of different temperatures. Ebrahimi and Roohi [27] investigated pressure-driven flows in diverging micro- and nanochannels. The flow field characteristics of diverging micro- and nanochannels are presented. The effects of various divergence angles on the flow and thermal field are analyzed [28]. The thermal field obtained was analyzed by numerical simulation. Experiments and three-position numerical simulation were carried out [29]. The flow rules of nitrogen in diverging micro- and nanochannels under different conditions are given [30]. Although the above microchannels can improve the gas transportation capacity, their configurations and temperature settings are complicated and not easy to process and manufacture. There is an urgent need to propose and investigate a microchannel with a simple structure that can improve gas transportation performance.

This paper presents a microchannel with constant and different temperature quadrangles inside. The microchannel is free from the limitation of needing to set temperature gradients on the same wall and different temperatures at different walls of the same component, i. e., each quadrilateral only needs to maintain the same fixed temperature, which reduces the difficulty of industrial manufacturing. The gas-induced mechanism of this microchannel is thermal-creep-like flow. The flow mechanism of thermal-creep-like flow is similar to that of thermal creep flow. The difference between them is that there is no temperature gradient on the drive wall and the temperature only needs to be kept constant. The difficulty of temperature control is reduced. Numerical simulations of the flow characteristics within the microchannel are investigated using the DSMC (Direct Simulation Monte Carlo) method. The effects of Knudsen number, quadrilateral aspect ratio, and column spacing on its gas transport capacity are analyzed. Section 2 describes the structural, temperature, and other parameters of the microchannel. Section 3 briefly describes the numerical simulation methods and calculations. Section 4 shows the verification of the independence of the parameters affecting the accuracy of the numerical simulation results. In section 5, the effects of Knudsen number, quadrilateral aspect ratio, and column spacing on the gas transport characteristics are analyzed. Section 6 gives the corresponding conclusions. This study provides qualitative evidence for the gas-pumping capability of the device. It provides a theoretical basis for the development and design of gas sensors in automobiles in the future.

2. Problem Statement

In this paper, the flow process of helium inside a two-dimensional microchannel with different temperature quadrilaterals is investigated. The quadrilateral in a microchannel is the cross-section of a quadrilateral prism. It is assumed that the length of a quadrilateral is much larger than its cross-section size. Therefore, only the numerical simulation of a two-dimensional structure can reasonably characterize the pumping capability of microchannels. Figure 1a schematically shows the structure of the microchannel. The microchannel comprises a series of neatly arranged low- and high-temperature quadrilaterals. The temperature of the low-temperature quadrilateral is T_c and that of the high-temperature quadrilateral is $T_h = T_c + 300$ K. The 300 K temperature difference is helpful for the study of gas pumping characteristics. The direction of the arrow indicates the direction of the gas flow. A low-temperature quadrilateral and its neighboring high-temperature quadrilateral in the microchannel are treated as one unit. In this paper, one of the units is studied to meet research objectives. Figure 1b shows the computational domain for numerical simulation. The computational domain contains a complete unit and one-half of two units adjacent to its top and bottom. The width of the high- and low-temperature quadrilateral is a and the height of the quadrilateral is b. In each row, the distance between two neighboring different temperature quadrilaterals is d. In each column, the distance between two neighboring same-temperature quadrilaterals is h. The top and bottom of the computational domain have symmetric boundaries. The left and right sides of the computational domain are periodic boundaries. The distance between the quadrilateral and the periodic boundary is L. Table 1 shows the values of each parameter in the computational domain.

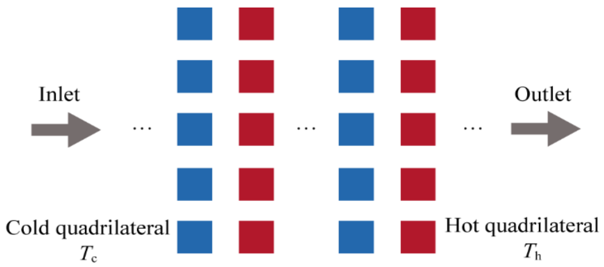

(a) Schematic diagrams of microchannels

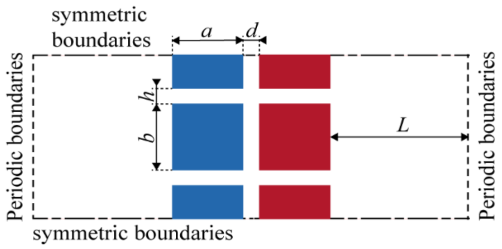

(b) Schematic diagrams of computational domains

Figure 1. Schematic diagrams of (**a**) microchannels and (**b**) computational domains.

Table 1. Calculation domain parameters.

Parameter	Value
Width of the quadrilateral a (m)	4×10^{-7}
Height of the quadrilateral b (m)	4×10^{-7}
Distance between different temperature quadrilaterals d (m)	10^{-7}
Distance between same temperature quadrilaterals h (m)	10^{-7}
Distance between the quadrilateral and the periodic boundary L (m)	8×10^{-7}
Low temperature T_c (K)	300
High temperature T_h (K)	600

3. Numerical Method and Computations

Thermally-induced flows in microchannels are dominated by transitional flows. The conventional Navier-Stokes (NS) equations cannot effectively solve such problems. The results obtained by using the Boltzmann equation are more accurate and reliable. In view of the complexity of the Boltzmann equation, various simplified forms of the Boltzmann equation are used in the research. The DSMC method uses many particles to simulate real gas molecules, and the solution of the Boltzmann equation is obtained by counting the particles [31]. The computational results of the DSMC method have been verified to be consistent with those of the experimental data [32]. It has become one of the main numerical simulation methods for solving rarefied gas flow problems [33]. Similar to the traditional computational fluid dynamics (CFD) methods, the computational domain of the DSMC method needs to be divided into grid cells. The macroscopic flow characteristics of the gas flow are then obtained by sampling and counting the particles within each grid cell. In the DSMC method, each DSMC particle represents many physical atoms or molecules. At the beginning of the computation, the simulated particles are uniformly distributed in the grid cells. As the time step advances, the particles move at their respective velocities, collide with each other, or interact with the boundary, and are then sampled and counted.

To obtain accurate numerical simulation results, several working parameters need to be set in the DSMC solver. In this study, the no-time-counter (NTC) collision method [34,35] is used to select collision pairs for calculation. Numerical simulations are carried out with the help of the DSMC solver, dsmcFoam+ [32], published in the object-oriented CFD open-source program OpenFOAM (Open Source Field Operation and Manipulation). In this program, a variable hard sphere (VHS) model is used to describe the intermolecular collision process [33]. The VHS model addresses significant limitations inherent in the Hard Sphere (HS) model, specifically the inability to simultaneously account for finite collision cross-sections and the temperature dependence of viscosity coefficients. While the VHS model maintains consistency with the HS model in terms of particle scattering mechanics, it introduces a critical modification: the collision cross-section is defined as a function of the relative velocity between particles. This innovative approach retains the computational simplicity of the uniform scattering law characteristic of the HS model, facilitating straightforward sampling procedures. Notably, research has demonstrated that while the specific mode of particle scattering exerts minimal influence on the flow field, the temperature-dependent viscosity coefficient significantly impacts flow dynamics [33]. This finding underscores the importance of accurately modeling temperature effects in molecular collision simulations. The efficacy and accuracy of the VHS model have been substantiated through extensive empirical and theoretical investigations. These studies have consistently validated the model's capacity to provide more accurate representations of molecular interactions across diverse flow regimes, particularly in scenarios where temperature-dependent viscosity plays a crucial role in determining flow characteristics [9,10,12,19,25].

The number of simulated particles in each of the divided grids is controlled to be more than 20. The maximum size of the grid should not be larger than $\lambda/3$, and λ is the mean free path of motion of helium molecules, which can be obtained from the following equation:

$$\lambda = \frac{k_B T}{\sqrt{2}\,\pi p_0 \theta^2}\left(\frac{T}{T_{\mathrm{ref}}}\right)^{\omega - 0.5} \tag{1}$$

where $\theta = 2.33 \times 10^{-10}\,\mathrm{m}$ is the reference diameter of the helium molecule in the VHS model, $T_{\mathrm{ref}} = 300\,\mathrm{K}$ is the reference temperature, and ω is the viscosity index, which is 0.66 for the standard case (101,325 Pa and 0 °C) of helium. In addition, the time step of the simulation should be smaller than e/u_0, where $u_0 = \sqrt{2k_B T_c/m}$ is the characteristic velocity of the particles in the microchannel, $m = 6.65 \times 10^{-27}\,\mathrm{kg}$ is the molecular mass of helium, and k_B is the Boltzmann constant.

In this paper, the variation of the dimensionless temperature T/T_c, flow pattern and dimensionless velocity u/u_0 of the gas flow in a microchannel with the Knudsen number Kn and dimensionless quadrilateral aspect ratio a/b is investigated. The Knudsen number can be obtained from the following equation:

$$Kn = \frac{\lambda}{W_{\mathrm{eff}}} \tag{2}$$

where W_{eff} is the characteristic size of the gas flow and can be obtained from the following equation:

$$W_{\text{eff}} = 2h + 2b - \frac{4ab}{2a+b} \tag{3}$$

4. Validation

In the DSMC method, cell size, time step, and the number of simulated particles per cell (PPC) affect the accuracy of the numerical simulation results [36−38]. This section verifies the independence of the cell size, time step, and PPC values on the effect of the numerical simulation results, respectively. Figure 2 shows the numerical simulation results for dimensionless temperature and number density for different cell sizes, time steps, and PPCs. Figure 2a, d show numerical simulation results for cell sizes of 10 nm (fine mesh), 20 nm (standard mesh), and 40 nm (coarse mesh), where the standard meshes are used for the numerical simulation in this paper. There is little difference in the results obtained according to the three precision cell sizes. Figure 2b, e shows numerical simulation results for time steps of 1 × 10^{-10} s, 1 × 10^{-11} s, and 1 × 10^{-12} s, where 1 × 10^{-11} s is the time step used in this paper. There is little difference in the results obtained according to the three precision time steps. Figure 2c, f shows the numerical simulation results for PPCs of 10, 20, and 40, where the value of PPC used in the numerical simulations is 20. There is little difference in the results obtained from the three different precision PPCs. The results demonstrate that the numerical predictions are independent of the computational grid size, time step, and the PPC.

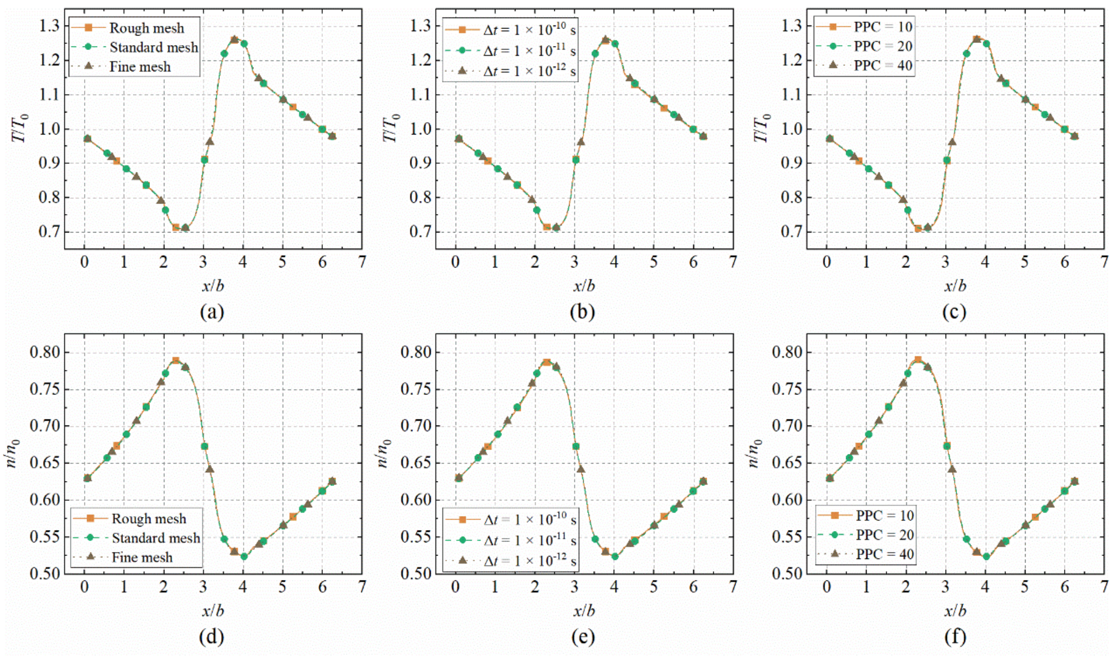

Figure 2. Dimensionless temperature and number density results obtained from numerical simulations at different cell sizes, time steps, and PPCs. (**a**) dimensionless temperature at different cell sizes; (**b**) dimensionless temperature at different time steps; (**c**) dimensionless temperature at different PPCs; (**d**) number density at different cell sizes; (**e**) number density at different time steps; (**f**) number density at different PPCs.

5. Results and Discussion

5.1. Knudsen Number

In this section, the effect of the Knudsen number on the microchannel gas flow characteristics is investigated. Figure 3 shows the temperature contours and velocity streamlines at different Knudsen numbers. The temperature distribution within the microchannel exhibits independence from the Knudsen number. Specifically, across the entire spectrum of Knudsen numbers, the highest temperatures are consistently observed in the regions between high-temperature quadrilaterals, while the lowest temperatures are consistently found in the areas between low-temperature quadrilaterals. This phenomenon can be attributed to the fact that the temperature profile within the microchannel is predominantly determined by the temperature of the quadrilateral walls. The underlying mechanism for this temperature distribution can be explained by molecular kinetics. Gas molecules that collide with high-temperature walls undergo an increase in kinetic energy, resulting in higher local temperatures. Conversely, molecules that interact with low-temperature walls experience a reduction in kinetic energy, leading to lower local temperatures. This molecular-level energy exchange process is the primary driver of the observed temperature gradients within the microchannel, regardless of the prevailing Knudsen number regime. The temperature gradient is markedly affected by the Knudsen number. As the Knudsen number increases, the temperature gradient of the gas decreases. This is because the gas becomes increasingly rarefied as the Knudsen number increases. The total probability of gas particles colliding with the wall is reduced, thereby decreasing the rate of heat exchange with the wall. As a consequence, the energy gained by the gas from the wall is diminished, and the temperature of the gas is reduced. A reduction in the temperature of the gas results in a corresponding decrease in the temperature gradient, which in turn leads to a weakening of the thermal-creep-like flow.

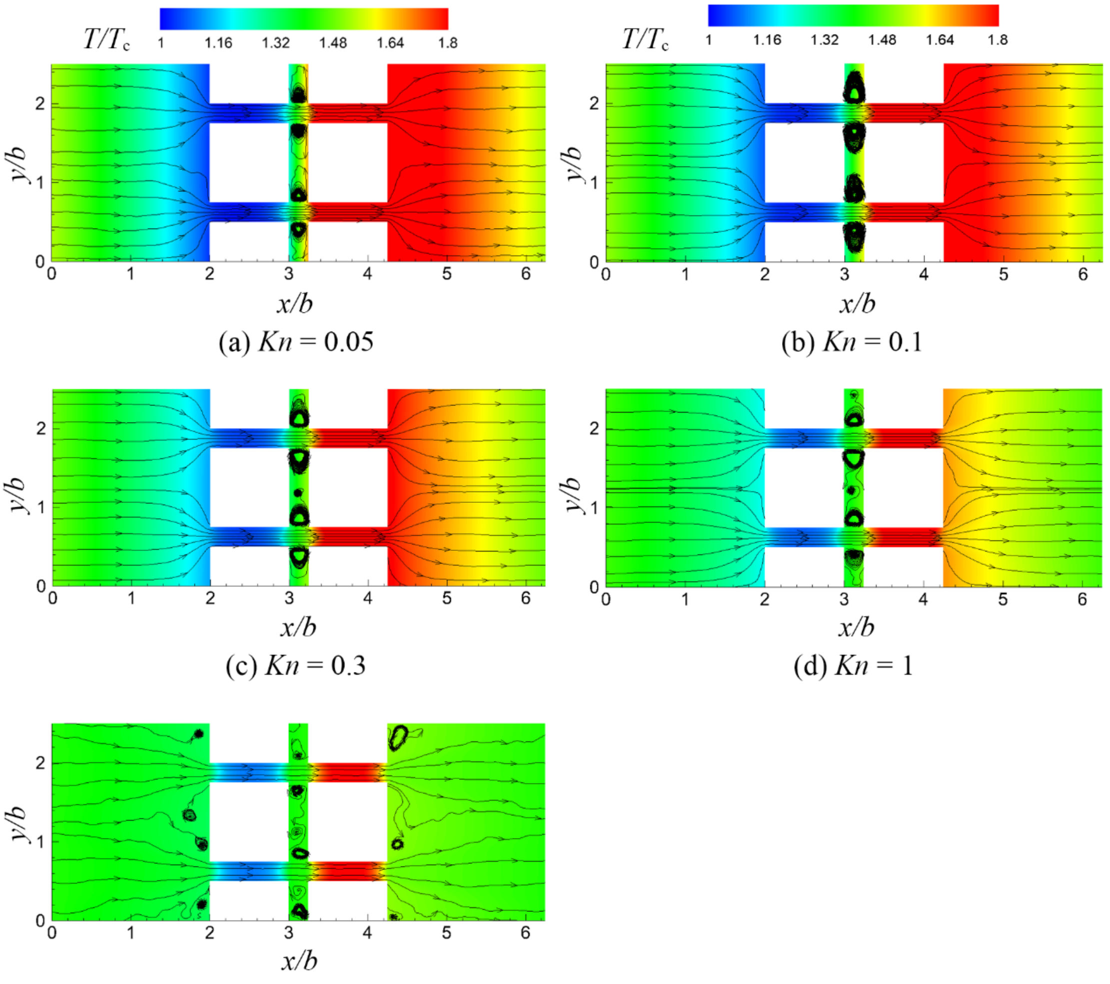

(a) $Kn = 0.05$

(b) $Kn = 0.1$

(c) $Kn = 0.3$

(d) $Kn = 1$

(e) $Kn = 10$

Figure 3. Temperature contours and streamlines with different Knudsen numbers.

The orientation of velocity streamlines demonstrates invariance with respect to the Knudsen number. Specifically, across the entire spectrum of Knudsen numbers, the velocity streamlines consistently maintain a directional flow from the vicinity of low-temperature quadrilaterals towards high-temperature quadrilaterals. This phenomenon can be attributed to the fact that the direction of velocity streamlines is fundamentally governed by the temperature gradient within the system. The temperature gradient, in turn, is determined by the temperature distribution across the quadrilateral surfaces. Given that the temperature differential between the quadrilaterals remains constant, the direction of the temperature gradient remains unaltered. Consequently, the directional characteristics of the velocity streamlines exhibit stability across varying Knudsen number regimes. When the Knudsen number is relatively low, the velocity streamline is observed to be smoother. But at $Kn = 10$, the velocity streamlines become irregular and chaotic, forming numerous vortices on the left and right sides of the quadrilateral. This is attributed to the diminished strength of the thermal-creep-like flow, which in turn reduces the driving force on the gas particles, resulting in a lower gas flow velocity. Concurrently, the gas is too rarefied, leading to a significant decline in gas particles.

Figure 4 illustrates the velocity distribution curves at varying Knudsen numbers. The velocity values close to the high- and low-temperature quadrilaterals are markedly elevated, whereas the velocity values on either side of the microchannel are considerably diminished. This is because the temperature gradient near the quadrilateral is considerably more pronounced than that observed on either side of the microchannel. Similarly, the velocity near the high-temperature quadrilateral is markedly higher than that near the low-temperature quadrilateral. As illustrated in Figure 3, an increase in temperature near the high-temperature quadrilateral is associated with a reduction in the Knudsen number. Figure 4, however, demonstrates that the velocity of the gas flow does not increase proportionately to the decrease in the Knudsen number. Instead, the velocity reaches its maximum value at $Kn = 0.3$. In the regime where the Knudsen number exceeds 0.3, a notable inverse relationship is observed between gas flow velocity and increasing Knudsen number. This phenomenon is particularly pronounced at $Kn = 10$, where gas flow velocities approach negligible levels, even in close proximity to quadrilateral boundaries. This behavior can be attributed to the progressive rarefaction of the gas as the Knudsen number increases, facilitating a transition from the transitional flow regime to free molecular flow. The rarefaction process diminishes molecular population density, consequently reducing the probability of wall collisions. This decrease in collision frequency reduces momentum and energy exchange between gas molecules and wall surfaces. The cumulative effect manifests as an attenuation of thermal-creep-like flow, ultimately resulting in decreased gas flow velocities. Conversely, in the regime where $Kn < 0.3$, gas flow velocities exhibit a similar declining trend with decreasing Knudsen numbers. This phenomenon can be explained by the transition from transitional to continuum flow as the Knudsen number decreases. It is important to note that thermal-creep-like flow are predominantly observed under rarefied gas conditions. As the gas approaches continuum flow, the mechanisms driving gas flow become less pronounced, leading to a reduction in overall gas flow velocities.

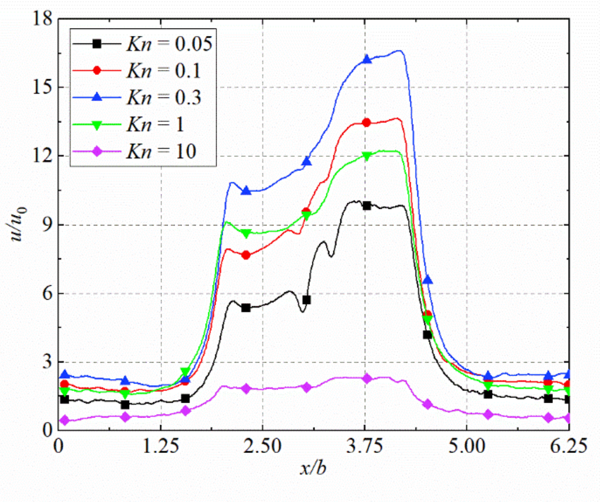

Figure 4. Velocity distribution curves with different Knudsen numbers.

5.2. Quadrilateral Aspect Ratio

In this section, the effect of the quadrilateral aspect ratio on gas flow characteristics is investigated. Figure 5 illustrates the temperature contours and velocity streamlines for different quadrilateral aspect ratios. The temperature distribution within microchannels exhibits independence from the aspect ratio of the constituent quadrilaterals. Consistently, the highest temperatures are observed in regions between high-temperature quadrilaterals, while the lowest temperatures are found in areas between low-temperature quadrilaterals. This phenomenon is attributed to the fact that the temperature profile within the microchannel is primarily determined by the temperature of the quadrilateral walls. Gas molecules acquire higher energy upon collision with high-temperature walls and lower energy upon interaction with low-temperature walls.

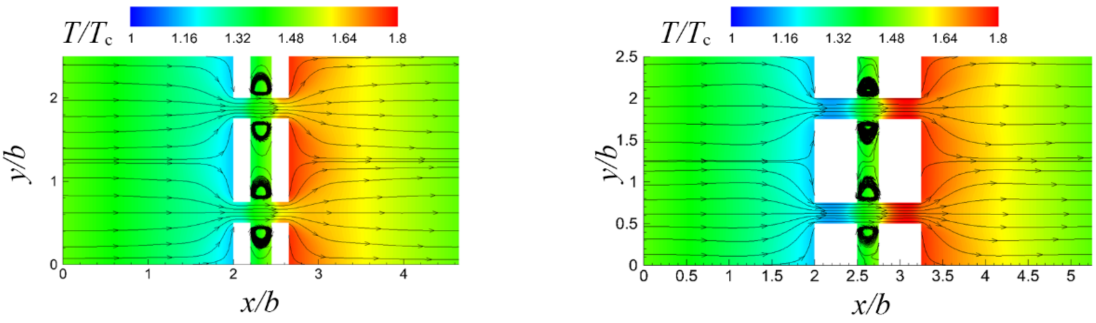

(a) $a/b = 0.2$ (b) $a/b = 0.5$

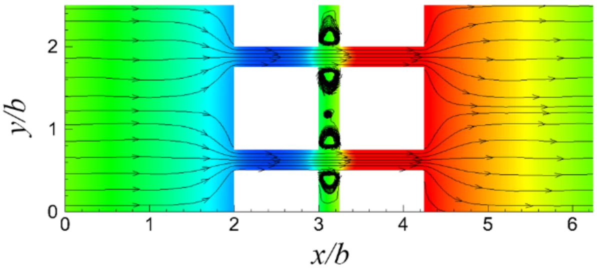

(c) $a/b = 1$

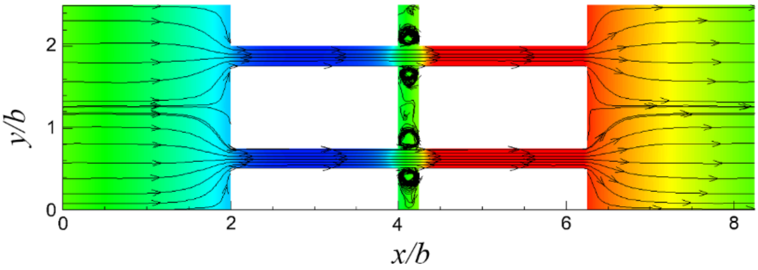

(d) $a/b = 2$

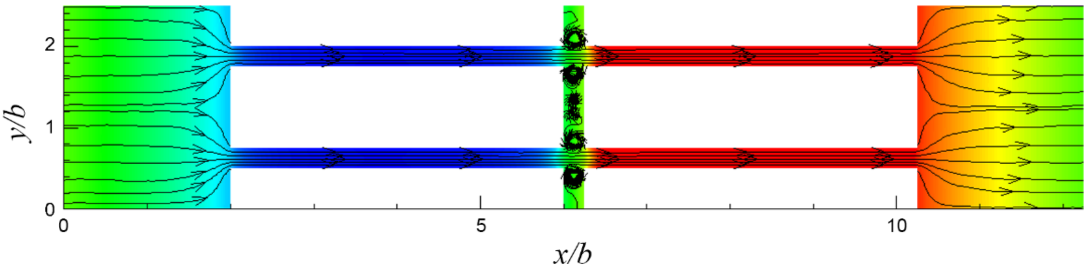

(e) $a/b = 4$

Figure 5. Temperature contours and streamlines with different quadrilateral aspect ratios.

However, the temperature gradient is significantly influenced by the quadrilateral aspect ratio. In configurations with small aspect ratios, the proximity between high and low-temperature quadrilaterals, coupled with a constant temperature difference, results in steep temperature gradients within the microchannel. Conversely, large aspect ratios, characterized by greater distances between high and low-temperature quadrilaterals, lead to more gradual temperature gradients while maintaining the same overall temperature difference.

The directionality of velocity streamlines remains unaffected by variations in the quadrilateral aspect ratio. Irrespective of the aspect ratio, velocity streamlines consistently originate from the vicinity of low-temperature quadrilaterals and progress towards high-temperature quadrilaterals. This directional consistency is a consequence of the temperature gradient, which is fundamentally determined by the temperature distribution across the quadrilateral surfaces. Preserving the temperature differential between quadrilaterals ensures the constancy of the temperature gradient direction, thereby maintaining the orientation of the velocity streamlines.

Figure 6 depicts the velocity distribution curves for varying quadrilateral aspect ratios. The velocity is high near the high- and low-temperature quadrilateral, while the velocity on either side of the microchannel is relatively low. This is due to the large temperature gradient near the quadrilateral. Furthermore, the velocity near the high-temperature quadrilateral is also markedly higher than that observed near the low-temperature quadrilateral. This is because the temperature gradient is larger near the high-temperature quadrilateral than near the low-temperature quadrilateral. As the aspect ratio of the quadrilateral increases, the flow velocity decreases. This is because an increase in the quadrilateral aspect ratio reduces the temperature gradient at a constant temperature. This results in a reduction in the intensity of thermal-creep-like flow, accompanied by a corresponding decrease in flow velocity. As the velocity decreases, the velocity streamline becomes increasingly irregular. Consequently, the velocity streamline becomes increasingly irregular as the quadrilateral aspect ratio increases. At $a/b = 4$, the velocity of the flow in the vicinity of the high-temperature quadrilateral is nearly identical to the velocity on both sides of the microchannel. At this juncture, the thermal-creep-like flow effect is essentially negligible.

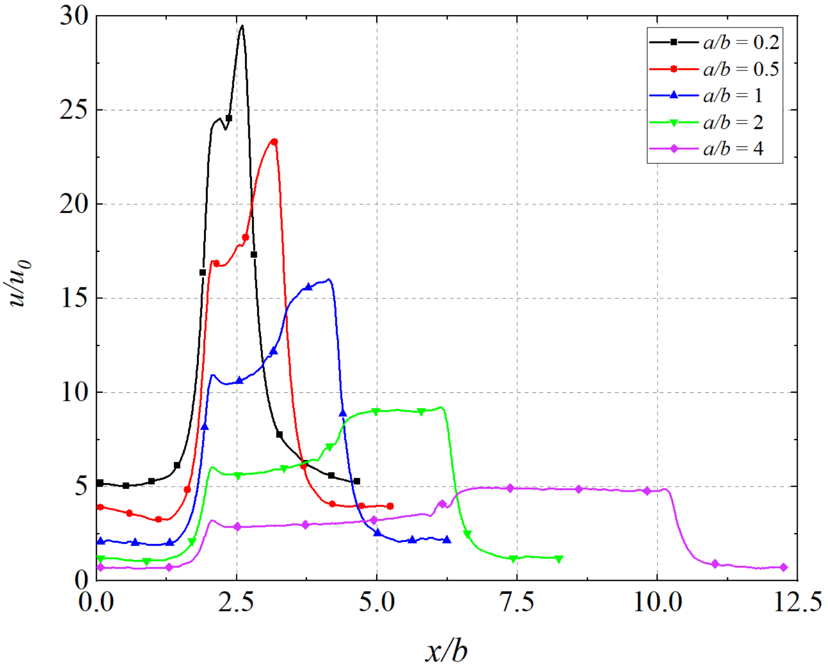

Figure 6. Velocity distribution curves with different quadrilateral aspect ratios.

6. Conclusions

In this paper, the gas flow characteristics in a microchannel are investigated using numerical simulation. The microchannel contains two quadrilateral columns with disparate temperatures. The mechanism of the gas flow is that of thermal-creep-like flow. The impact of the Knudsen number and quadrilateral aspect ratio on the gas flow characteristics is examined. It is demonstrated that the gas flowed from the low-temperature quadrilateral to the high-temperature quadrilateral within the microchannel. The capacity of the microchannels to pump gases is demonstrated. The maximum gas flow rate is observed at Knudsen number equal to 0.3, which is influenced by the intensity of thermal-creep-like flow and the number of gas molecules. At this juncture, the gas flow can be classified as transitional flow. This suggests that the microchannel exhibits the greatest gas pumping capacity in the transitional flow. As the aspect ratio of the quadrilateral increases, the flow rate declines.

Author Contributions: L. H.: Conceptualization, Investigation, Data curation, Methodology, Validation, Visualization, software, Writing—original draft, Writing—review & editing. F.H.: Supervision, Project administration, Writing—review & editing, Resources, software. R.L.: Validation, Data curation, Conceptualization. J.S.: Supervision, Funding acquisition, Project administration, Resources. D. Z.: Validation, Data curation, Visualization, Funding acquisition. Y. S.: Funding acquisition, Resources. K. S.: Funding acquisition, Conceptualization. All authors have read and agreed to the published version of the manuscript.

Funding: This research was funded by the National Natural Science Foundation of China (No. 12002142, 52305240), the Shandong Provincial Natural Science Foundation of China (Grant NO. ZR2022ME082, ZR2021QB137), the Youth Entrepreneurship Technology Support Program for Higher Education Institutions of Shandong Province (No. 2023KJ215), the Scientific Research of Linyi University (No. 2021PTXM001, Z620622003).

Institutional Review Board Statement: Not applicable.

Informed Consent Statement: Not applicable.

Data Availability: Statement: Not applicable.

Conflicts of Interest: The authors declare no conflict of interest.

References

1. Moos, R. A Brief Overview on Automotive Exhaust Gas Sensors Based on Electroceramics. *Int. J. Appl. Ceram. Technol.* **2005**, *2*, 401–413.
2. Liu H.; Li M.; Voznyy O.; Hu L.; Fu Q.; Zhou D.; Xia Z.; Sargent E.H.; Tang J. Physically flexible, rapid-response gas sensor based on colloidal quantum dot solids. *Adv. Mater.* **2014**, *26*, 2718–2724.
3. Raghavan A.; Kiesel P.; Sommer L. W.; Schwartz J.; Lochbaum A.; Hegyi A.; Schuh A.; Arakaki K.; Saha B.; Ganguli A. et al. *Embedded fiber-optic sensing for accurate internal monitoring of cell state in advanced battery management systems part* **1**: Cell embedding method and performance. *J. Power Sources* **2017**, *341*, 466–473.
4. Ganguli A.; Saha B.; Raghavan A.; Kiesel P.; Arakaki K.; Schuh A.; Schwartz J.; Hegyi A.; Sommer L. W.; Lochbaum A.; et al. Embedded fiber-optic sensing for accurate internal monitoring of cell state in advanced battery management systems part 2: Internal cell signals and utility for state estimation. *J. Power Sources* **2017**, *341*, 474–482.
5. Bond D. M.; Wheatley V.; Goldsworthy M. Numerical investigation into the performance of alternative Knudsen pump designs. *Int. J. Heat Mass Transf.* **2016**, *93*, 1038–1058.
6. Kosyanchuk V.; Kovalev V.; Yakunchikov A. Multiscale modeling of a gas separation device based on effect of thermal transpiration in the membrane. *Sep. Purif. Technol.* **2017**, *180*, 58–68.
7. Taguchi S.; Aoki K. Rarefied gas flow around a sharp edge induced by a temperature field. *J. Fluid Mech.* **2012**, *694*, 191–224.
8. Yakunchikov A.; Kosyanchuk V. Numerical investigation of gas separation in the system of filaments with different temperatures. *Int. J. Heat Mass Transf.* **2019**, *138*, 144–151.
9. Baier T.; Hardt S. Gas separation in a Knudsen pump inspired by a Crookes radiometer. *Microfluid. Nanofluidics* **2020**, *24*, 41.
10. Lotfian A.; Roohi E. Radiometric flow in periodically patterned channels: Fluid physics and improved configurations. *J. Fluid Mech.* **2019**, *860*, 544–576.
11. Baier T.; Hardt S.; Shahabi V.; Roohi E. Knudsen pump inspired by Crookes radiometer with a specular wall. *Phys. Rev. Fluids* **2017**, *2*, 033401.
12. Lotfian A.; Roohi E. Binary gas mixtures separation using microscale radiometric pumps. *Int. Commun. Heat Mass Transf.* **2021**, *121*, 105061.
13. Aoki K.; Degond P.; Mieussens L.; Takata S.; Yoshida H. A Diffusion Model for Rarefied Flows in Curved Channels. *Multiscale Model. Simul.* **2008**, *6*, 1281–1316.
14. Bond D.M.; Wheatley V.; Goldsworthy M. Numerical investigation of curved channel Knudsen pump performance. *Int. J. Heat Mass Transf.* **2014**, *76*, 1–15.
15. Donkov A.A.; Tiwari S.; Liang T.; Hardt S.; Klar A.; Ye W. Momentum and mass fluxes in a gas confined between periodically structured surfaces at different temperatures. *Phys. Rev. E* **2011**, *84*, 16304.
16. Wurger, A. Leidenfrost gas ratchets driven by thermal creep. *Phys. Rev. Lett.* **2011**, *107*, 164502.

17. Chen J.; Baldas L.; Colin S. Numerical study of thermal creep flow between two ratchet surfaces. *Vacuum* **2014**, *109*, 294–301.
18. Chen J.; Stefanov S. K.; Baldas L.; Colin S. Analysis of flow induced by temperature fields in ratchet-like microchannels by Direct Simulation Monte Carlo. *Int. J. Heat Mass Transf.* **2016**, *99*, 672–680.
19. Shahabi V.; Baier T.; Roohi E.; Hardt S. Thermally induced gas flows in ratchet channels with diffuse and specular boundaries. *Sci. Rep.* **2017**, *7*, 41412.
20. Tatsios G.; Lopez Quesada G.; Rojas-Cardenas M.; Baldas L.; Colin S.; Valougeorgis D. Computational investigation and parametrization of the pumping effect in temperature-driven flows through long tapered channels. *Microfluid. Nanofluid.* **2017**, *21*, 99.
21. Gupta N. K.; Gianchandani Y. B. Thermal transpiration in mixed cellulose ester membranes: Enabling miniature, motionless gas pumps. *Microporous Mesoporous Mat.* **2011**, *142*, 535–541.
22. Han F.; Wang X.; Zhao F.; Zhang S.; Zhang Z. Numerical investigation of gas separation via thermally induced flows in ratchet-like patterned microchannels. *Int. J. Therm. Sci.* **2022**, *172*, 107280.
23. Han F.; Wang X.; Zhang W.; Zhang S.; Zhang Z. Gas separation simulation based on ab initio and variable soft sphere model in ratchet-shaped microchannels. *Int. J. Heat Mass Transf.* **2023**, *206*, 123957.
24. Han F.; Zhang Z.; Zhang, S.; Wang, X. Simulation Study of the Effect of Surface Properties on Gas Separation Characteristics for Ratchet-type Knudsen Pumps. *Vacuum* **2024**, *61*, 13–19.
25. Wang X.; Zhang Z.; Zhang W.; Zhang P.; Zhang S. Numerical simulation of thermal edge flow in ratchet-like periodically patterned micro-channels. *Int. J. Heat Mass Transf.* **2019**, *135*, 1023–1038.
26. Han F.; Wang X.; Zhang, W.; Zhang, S.; Zhang, Z. Numerical Simulation Optimization via DSMC Method for Thermally Induced Flow in Microchannel-Type Knudsen Pumps with Quadrilateral Arrays. *Chin. J. Vac. Sci. Technol.* **2023**, *43*, 238–244.
27. Ebrahimi A.; Roohi E. DSMC investigation of rarefied gas flow through diverging micro- and nanochannels. *Microfluid. Nanofluid.* **2017**, *21*, 1.
28. Ebrahimi A.; Roohi E. Flow and Thermal Fields Investigation in Divergent Micro/Nano Channels. *J. Therm. Eng.* **2018**, *2*, 709–714.
29. Ebrahimi A.; Shahabi V.; Roohi E. Pressure-Driven Nitrogen Flow in Divergent Microchannels with Isothermal Walls. *Appl. Sci.* **2021**, *11*, 3602.
30. Varade V.; Duryodhan V.S.; Agrawal A.; Pradeep A.M.; Ebrahimi A.; Roohi E. Low Mach number slip flow through diverging microchannel. *Comput. Fluids* **2015**, *111*, 46–61.
31. Scanlon T.J.; Roohi E.; White C.; Darbandi M.; Reese J.M. An open source, parallel DSMC code for rarefied gas flows in arbitrary geometries. *Comput. Fluids* **2010**, *39*, 2078–2089.
32. White C.; Borg M. K.; Scanlon T. J.; Longshaw S. M.; John B.; Emerson D. R.; Reese J. M. DsmcFoam+: An OpenFOAM based direct simulation Monte Carlo solver. *Comput. Phys. Commun.* **2018**, *224*, 22–43.
33. Bird, G.A. *Molecular Gas Dynamics and the Direct Simulation of Gas Flow*; Clarendon Press: Oxford, UK, 1994.
34. Roohi E.; Stefanov S.; Shoja-Sani A.; Ejraei H. A generalized form of the Bernoulli Trial collision scheme in DSMC: Derivation and evaluation. *J. Comput. Phys.* **2018**, *354*, 476–492.
35. Roohi E.; Stefanov S. Collision partner selection schemes in DSMC: From micro/nano flows to hypersonic flows. *Phys. Rep.* **2016**, *656*, 1–38.
36. Zhu M.; Roohi E.; Ebrahimi A. Computational Study of Rarefied Gas Flow and Heat Transfer in Lid-driven Cylindrical Cavities. *Phys. Fluids* **2023**, *35*, 052012.
37. Sabouri M.; Zakeri R.; Ebrahimi A. Improving Computational Efficiency in DSMC Simulations of Vacuum Gas Dynamics with a Fixed Number of Particles per Cell. *Phys. Scr.* **2024**, *99*, 085213.
38. Shariati V.; Roohi E.; Ebrahimi A. Numerical Study of Gas Flow in Super Nanoporous Materials Using the Direct Simulation Monte-Carlo Method. *Micromachines* **2023**, *14,* 139.